SLU JST
Sule Lamido University Journal of Science & Technology Vol. 9 No. 1&2 [May, 2024], pp. 184-196
https://doi.org/10.56471/
Online ISSN: 2736-0903
Print ISSN: 2736-089X
www.slujst.edu.ng

Bridging Simulation and Experiment: Crystallite Size and Microstrain Analysis of Magnetite (Fe_3O_4) Nanoparticles

Abdulrazak Abubakar Isah[1,*], Ibrahim Garba Shitu[2], Dauda Muhammad[1], Suleiman Bashir Adamu[2], Kamil Kayode Katibi[3], Sani Garba Durumin Iya[2], Idris Muhammad Chiromawa[2]

[1]Bilyaminu Usman Polytechnic Hadejia, Jigawa State, 013 Hadejia, Jigawa State, Nigeria.
[2]Department of Physics, Faculty of Natural and Applied Science, Sule Lamido University Kafin Hausa, 048 Kafin Hausa, Jigawa State, Nigeria
[3]Department of Process and Food Engineering, Faculty of Engineering, Universiti Putra Malaysia, UPM Serdang, Selangor 43400, Malaysia.

*Corresponding author email: aabubakar819@gmail.com

Abstract

The determination of crystallite size of nanoparticles is a significant challenge due to the limitations of relying on a single estimation method. This study investigates the structural properties of synthesized Magnetite (Fe_3O_4) nanoparticles through a combination of experimental and simulated X-ray diffraction (XRD) analysis. Using VESTA software, a simulated XRD pattern was generated based on precise crystal structure details obtained from a CIF file, closely validating the high purity and crystallinity of the synthesized Fe_3O_4 nanoparticles. Various estimation methods, including Scherer's method, Size Strain Plot method, and Halder-Wagner method, were employed to estimate crystallite size and microstrain. Comparison of results from both experimental and simulated data revealed slight discrepancies attributed to differences in measurement techniques, sample preparation, and material properties. Additionally, Energy-Dispersive X-ray (EDX) analysis confirmed the composition of the synthesized nanoparticles, while transmission electron microscopy (TEM) and field emission scanning electron microscopy (FESEM) provided further validation of particle size. This study provides a comprehensive exploration of the structural properties of Magnetite (Fe_3O_4) nanoparticles, emphasizing the integration of multiple analysis techniques and simulation methods to enhance precision and reliability in estimating crystallite size. By combining experimental approaches with simulations, it offers a thorough understanding of the nanoparticles' composition and structural characteristics, contributing to advancements in nanomaterials research.

Keywords: *Magnetite (Fe_3O_4), Nanoparticle, Crystallite size, Microstrain, Simulation, Scherer's method.*

1. Introduction

Nanotechnology has recently garnered significant attention for its remarkable capacity to engineer, characterize, and finely tune the functional properties of nanostructures (Bilal et al., 2022). Metallic nanoparticles (NPs) hold particular interest due to their broad range of applications spanning from biomedical to electronic domains, encompassing areas such as biomedical treatments, ferrofluid materials, advanced magnetic materials, catalysts, groundwater remediation, hazardous waste treatment, coloured pigments, medical diagnostics, and magnetic recording media (Bilal et al., 2022; Vieira et al., 2020). At the nanoscale (ranging from 1 to 100 nm), particles exhibit distinct physical properties that significantly diverge from their larger, micron-sized counterparts (10-100 μm). These nanoscale particles exhibit diverse and intriguing attributes such as magnetic behaviour, optical properties, and surface reactivity, all inherently linked to their particle size. Thus, achieving precise determination

Online ISSN: 2736-0903
Print ISSN: 2736-089X
www.slujst.edu.ng

of crystallite size is imperative for gaining a comprehensive understanding of nanoscale material properties (Adeniyi et al., 2023; Mujtaba et al., 2023).

Iron, known for its abundance and versatility, holds a prominent position among the elements on Earth. In recent years, iron oxide nanoparticles have emerged with vast potential across diverse applications, including but not limited to magnetic fluids, catalysts for carbon nanotube synthesis, contrast agents in magnetic resonance imaging (MRI), and components in nickel-iron batteries and environmental remediation processes (Chen et al., 2023; Khan et al., 2020; Zahedifar et al., 2021). The versatility of iron nanoparticles lies in their ability to adopt various forms tailored to specific applications. For instance, aggregated nanosized iron powder finds utility in Ni-Fe batteries and environmental clean-up efforts, whereas well-dispersed colloidal iron is essential for applications in biological systems like MRI enhancement and biomaterials separation (Dong et al., 2022; Qu et al., 2022; Yang et al., 2021). In another significant application, the growth of carbon nanotubes on silicon substrates via chemical vapor deposition relies on iron, cobalt, or nickel nanoparticles as catalysts (Eltaweil et al., 2020; Yi et al., 2019). In such applications, achieving dispersive separation of nanoparticles on the substrate becomes crucial to prevent interference among nanotubes, particularly in field-emission sources. A plethora of synthesis methods have been reported for producing Fe_3O_4 nanoparticles, encompassing techniques such as co-precipitation, sol-gel processes, flow injection, electrochemical methods, solvothermal and hydrothermal routes, microwave-assisted synthesis, and thermal decomposition of iron (III) acetylacetonate in tri (ethylene glycol), among others (Wang et al., 2019; Yi et al., 2020). These methods offer a diverse array of approaches to tailor the properties and characteristics of iron oxide nanoparticles to suit specific application requirements and advance technological innovations (Jia et al., 2019).

Among the methodologies available for determining crystallite size, Scherrer's method stands as a well-established technique utilizing X-ray diffraction (XRD) patterns to compute the average size of crystallites based on diffraction peak width (Chin et al., 2022a). However, it's essential to recognize that Scherrer's formula provides only a lower limit estimation of crystallite size, as it fails to account for peak broadening contributions resulting from crucial factors like inhomogeneous strain and instrumental effects (Billah et al., 2023). In reality, both crystallite size and lattice strain contribute to the broadening of X-ray diffraction peaks in nanoparticles. This peak broadening, primarily attributed to lattice strain, arises from the substantial volume of grain boundaries in nanoparticles, potentially impacting the accurate determination of crystallite size (Sonmez et al., 2015). Therefore, conducting strain calculations becomes essential to achieve precise measurements of crystallite size and explore the influence of strain on nanomaterial properties (Kandemir et al., n.d.; Liu et al., 2020). In contrast to Scherrer's method, X-ray diffraction peak profile analysis (XPPA) incorporates the consideration of peak broadening stemming from factors like inhomogeneous strain and instrumental effects. This analytical approach has been widely utilized for determining grain size, lattice distortion, twinning, stacking fault probabilities, as well as long-range and root mean square stresses in nanocrystalline materials. Various XPPA techniques, including the Williamson-Hall methods, Stress-Strain Plot Methods, and Halder Wagner Methods, have been employed to estimate crystallite size and lattice strain based on X-ray peak broadening (Kumar et al., 2021; Kushwaha & Chauhan, 2021; Shweta et al., 2021).
The primary aim of this research is to accurately determine the crystallite size of nanocrystalline hematite nanoparticles through a comprehensive analysis of powder X-ray diffraction (XRD) data. In addition to analyzing experimental XRD data, the study will utilize VESTA software for simulating results, allowing for a comparison between simulated and experimental data to confirm the accuracy of the calculated crystallite size. Furthermore, the research aims to extend its analysis by comparing the determined crystallite size with particle size distributions obtained from Transmission Electron Microscopy (TEM) analyses. This approach ensures robust validation of the crystallite size derived from XRD data and contributes to a deeper understanding of the structural properties of hematite nanoparticles. Through this multifaceted methodology, the study aims to provide valuable insights into nanomaterial characterization, advancing knowledge in this field.

SLU JST
Sule Lamido University Journal of Science & Technology Vol. 9 No. 1&2 [May, 2024], pp. 184-196
https://doi.org/10.56471/
Online ISSN: 2736-0903
Print ISSN: 2736-089X
www.slujst.edu.ng

2. Materials and Method

2.1 Materials

The materials used in the present research include iron (III) nitrate hydrate Fe $(NO_3)_3 \cdot 9H_2O$ (MW: 404.00; CAS: 7782- 61-8), anhydrous citric acid ($C_6H_8O_7.H_2O$) (M_W: 192.12; CAS: 77-92-9), as starting materials and were of analytical grade. Distilled water was used to prepare aqueous solutions during the whole experiment.

2.2 Methods

2.2.1 Synthesis of Magnetite (Fe_3O_4) using Auto-Combustion Technique

Magnetite (Fe_3O_4) nanoparticles via the solution combustion method, ferric nitrate was initially dissolved in 5 mL of distilled water with continuous stirring at room temperature. Simultaneously, the fuel was dissolved in another 5 mL of distilled water. Subsequently, the two solutions were meticulously mixed until a homogeneous solution was achieved. This uniform mixture was then heated at 400°C for 30 minutes in a furnace to yield the Fe_3O_4 nanoparticles. The resulting product was further ground to obtain Fe_3O_4 nano powder.

2.2.2 Simulation of Magnetite (Fe_3O_4) using Vesta Software

In this study, the simulation of X-ray diffraction (XRD) graphs for magnetite nanoparticles using VESTA software was comprehensively obtained. The procedure commenced with the download and installation of VESTA software, followed by obtaining a CIF file containing accurate crystal structure details for magnetite nanoparticles. Subsequently, the CIF file was used in VESTA, and simulation parameters were set up including the specification of the X-ray wavelength and adjustments of other parameters to meet research requirements. The XRD simulation process was then initiated, leading to the generation of a simulated XRD pattern based on the specified parameters and the crystal structure of magnetite nanoparticles. Analysis of the simulated pattern facilitated the identification of peaks corresponding to magnetite's crystallographic planes. Moreover, comparison with experimental data enabled the validation of results, with necessary parameter adjustments made for accuracy. Finally, the simulated XRD pattern was saved and data exported for further analysis and documentation, providing a comprehensive simulated structural properties of magnetite's crystallographic structure.

3. Characterization

The X-ray diffraction (XRD) patterns were acquired using an X-ray diffractometer (X'pert Pro, Panalytical), with CuK radiation (λ=0.154187 nm), in the 2θ angle range of 20° to 80°. The collected XRD patterns were analyzed using the X'pert High Score Plus software (version 3.0e (3.0.5)). Surface properties of the prepared samples were analyzed using the ScanAsyst peak force tapping mode of the Bruker Dimension Edge atomic force microscopy (AFM). The morphology of the samples was further examined using field emission scanning electron microscopy (FESEM) (FEI Nova SEM230) at a working distance of 5.2 nm and an accelerating voltage of 10.0 kV. The elemental composition of the samples was characterized using an energy dispersive X-ray (EDX) spectrometer (7353, Oxford Instruments).

4. Result and Discussion

4.1 Structural Analysis

4.1.1 X-ray Diffraction (XRD)

The X-ray diffraction (XRD) profile of the synthesized magnetite nanoparticles is depicted in Figure 1(a), revealing distinct peaks observed at specific angles: 24.12°, 33.14°, 35.60°, 40.85°, 49.45°, 54.0°, 57.5°, 62.44°, 64.00°, 72.86°, and 75.35°. These peaks correspond to crystal planes (111), (220), (311), (222), (400), (422), (511), (440), (214), (300), (1010), and (220), respectively. Remarkably, the experimental diffraction planes closely align with the simulated diffraction pattern illustrated in Figure 1(b), indicative of a close match to the hexagonal Magnetite nanoparticle's stick pattern found in the International Crystallographic Diffraction Data (ICDD) under number 00-024-0072. Furthermore, the absence of any impurity in the diffractograms underscores the high purity of the

Sule Lamido University Journal of Science & Technology Vol. 9 No. 1&2 [May, 2024], pp. 184-196
https://doi.org/10.56471/
Online ISSN: 2736-0903
Print ISSN: 2736-089X
www.slujst.edu.ng

synthesized particles. The sharpness of the diffraction peaks in the XRD profile suggests the presence of highly crystalline particles. Leveraging this diffraction profile, essential parameters such as crystallite size, intrinsic strain, and stress of the nanoparticles will be calculated using various models, ensuring a comprehensive analysis of the structural properties of the synthesized magnetite nanoparticles. Thus, the alignment observed between the XRD diffraction patterns of both the experimental and simulated data confirms the structural integrity of the synthesized magnetite nanoparticles.

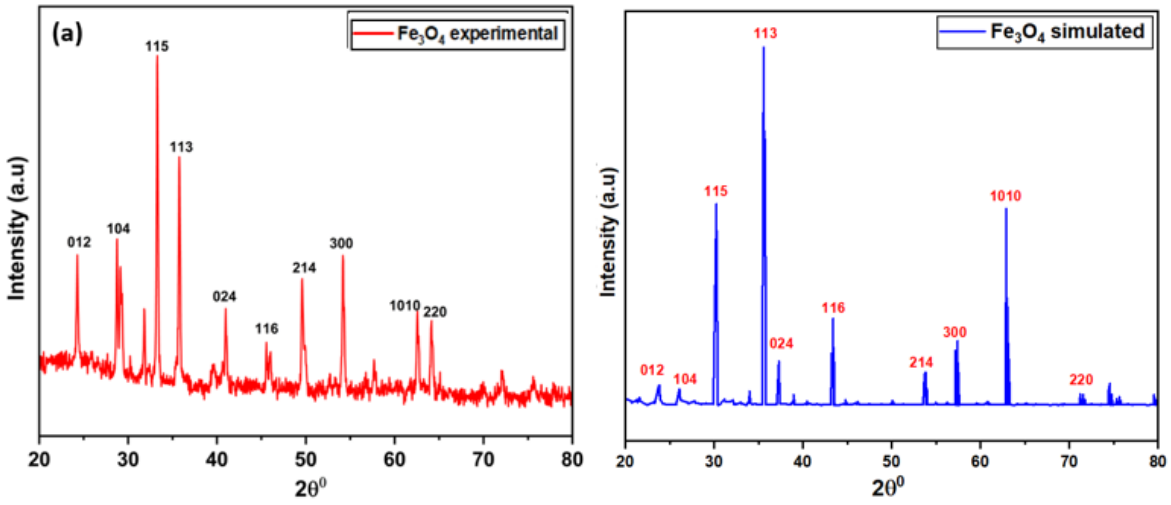

Figure 1: (a) XRD pattern of experimental Fe_3O_4 nanoparticle (b) XRD pattern of simulated Fe_3O_4 nanoparticle

4.1.1.1 Scherer's Method

Scherer's method, also known as the Scherrer equation or Scherrer's formula, is a widely used technique for estimating the crystallite size in a material from the broadening of x-ray diffraction peaks. This method provides valuable insights into the average size of the crystalline domains present in a sample (Abed et al., 2019). The Scherrer equation is derived from the fundamental principles of x-ray diffraction and makes use of the peak broadening resulting from the finite size of the crystalline domains. According to this equation, the crystallite size (D) is related to the peak broadening (β), the X-ray wavelength (λ), the Bragg angle (θ), and a dimensionless shape factor (K) (Basak et al., 2022):

$$D = \frac{k\lambda}{\beta_{hkl}\cos\theta} \quad (1)$$

where λ is the X-ray wavelength, k is the shape factor (usually taken as 0.9) β is the full width at half maximum (FWHM) of the diffraction peaks and θ is the Bragg's angle of reflection.

In applying Scherer's method to evaluate crystallite size, X-ray diffraction (XRD) measurements were conducted on Fe_3O_4 nanoparticles. The resulting XRD pattern provides critical information regarding the positions and intensities of diffraction peaks, which correspond to specific crystal planes within the material. The observed broadening of peaks is attributed to the finite size of the crystalline domains (Desai et al., 2021). Figure 2 shows graphs applying Scherer's method to both experimental and simulated Fe_3O_4 nanoparticles, along with the respective linear least square method equations derived from linear regression data plots. Notably, the estimated crystallite size and microstrain from the experimental data was 20.66 nm and 2.35×10^{-3}, whereas that from the simulated data notably exceeded it at 36.39 nm and 2.75×10^{-3} respectively. This discrepancy prompts investigation into various factors contributing to the observed difference. One potential explanation is the idealized nature of simulated data, which may not fully encapsulate the complexities and imperfections present in real-world samples. Simulated XRD

Sule Lamido University Journal of Science & Technology Vol. 9 No. 1&2 [May, 2024], pp. 184-196
https://doi.org/10.56471/
Online ISSN: 2736-0903
Print ISSN: 2736-089X
www.slujst.edu.ng

patterns are based on theoretical models and assumptions, diverging from the nuanced intricacies inherent in experimental data, which reflect the actual crystalline structure of synthesized nanoparticles, accounting for defects, grain boundaries, and strain (Aly et al., 2017). Additionally, discrepancies may arise from variations in sample preparation techniques, synthesis conditions, and measurement parameters(Sapna et al., 2018). Furthermore, it's important to acknowledge the limitations of the models used for crystallite size estimation in both simulated and experimental analyses, which may lead to differences in calculated crystallite size and microstrain. Hence, understanding these factors is crucial for interpreting and reconciling disparities between simulated and experimental assessments of crystallite size in XRD analysis.

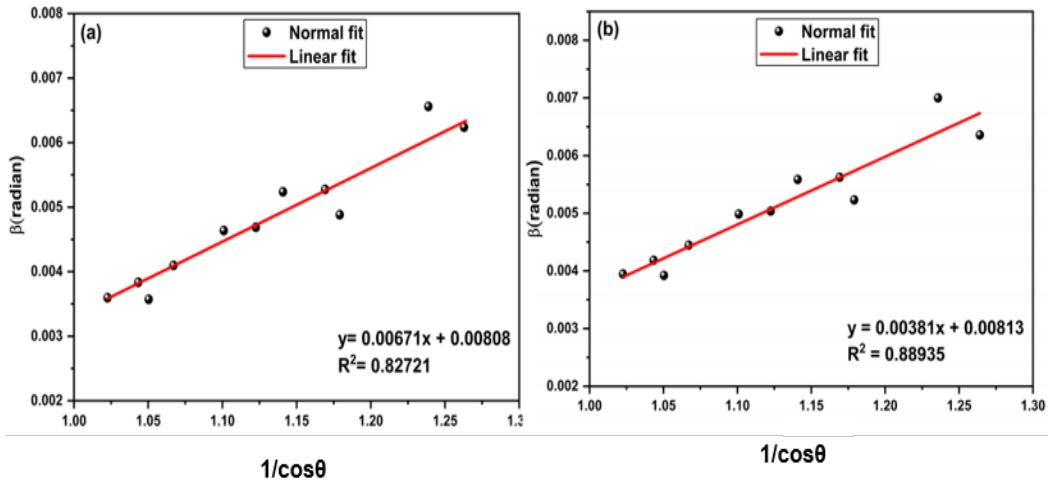

Figure 2: (a) Experimental Scherer's method estimated crystallite size of Fe_3O_4 nanoparticle (b) Simulated Scherer's method estimated crystallite size of Fe_3O_4 nanoparticle.

4.1.1.2 Size Strain Plot Method (SSP)

The Size Strain Plot method is a widely used technique for estimating the crystallite size and microstrain in a material based on X-ray diffraction (XRD) data. This method provides valuable information about the average size of the crystalline domains and the presence of any lattice distortions or microstrain within the material (Sapna et al., 2018). The Size Strain Plot method utilizes the analysis of peak broadening in XRD patterns. The broadening of the diffraction peaks arises from several factors, including the finite size of the crystalline domains and the presence of lattice distortions or microstrain. By quantifying the peak broadening, it is possible to determine both the average crystallite size and the microstrain within the material (Yousefi et al., 2022). Moreover, it is important to note that the Size Strain Plot method assumes an isotropic strain distribution within the crystalline domains. Also, accurate determination of the crystallite size and microstrain requires careful measurement and analysis of the XRD peaks, considering instrumental broadening and other factors that may affect the peak shape. As a result, the total peak broadening in the size-strain plot method (SSP) can be calculated using the formula as follows (Aly et al., 2016):

$$\beta_{hkl} = \beta_L + \beta_G \quad (2)$$

where β_L and β_G are Lorentzian and Gaussian Peak broadening. The SSP method separates the contributions of size and strain effects on the broadening of X-ray diffraction peaks. By considering both factors separately, it becomes easier to analyze and quantify the effects of isotropic enlargement (Monshi et al., 2012). Furthermore, the size strain plot (SSP) method consistently yields superior results when analyzing isotropic enlargement. This is attributed to its enhanced applicability to low angle reflections, where higher accuracy and precision are achieved compared to higher angles. The quality of X-ray diffraction (XRD) data tends to decrease at higher angles, leading to significant peak overlapping. In contrast, the lower diffraction angles provide clearer and more reliable information. The SSP calculation is performed using the following equation express as (Rani et al., 2019):

SLUJST
Sule Lamido University Journal of Science & Technology Vol. 9 No. 1&2 [May, 2024], pp. 184-196
https://doi.org/10.56471/
Online ISSN: 2736-0903
Print ISSN: 2736-089X
www.slujst.edu.ng

$$\left(d_{hkl}\beta_{hkl}\cos\theta\right)^2 = \frac{K\lambda}{D}\left(d_{hkl}^2\beta_{hkl}\cos\theta\right) + \frac{\varepsilon^2}{4} \quad (3)$$

where d_{hkl} is lattice separation between the lattice plane (hkl) of the hexagonal crystal structure. The lattice separation between the diffraction planes (hkl) can be calculated using the equation express as: The lattice separation between the diffraction planes (hkl) can be calculated using the equation express as (Gholizadeh, 2015):

$$\frac{1}{d_{hkl}^2} = \frac{4}{3}\left(\frac{h^2+hk+k^2}{a^2}\right) + \left(\frac{l^2}{c^2}\right) \quad (4)$$

$$d_{hkl}^2 = \left(\frac{a^2}{h^2+k^2+l^2}\right) \quad (5)$$

Therefore, a plot of $\left(d_{hkl}\beta_{hkl}\cos\theta\right)^2$ on y-axis and $\left(d_{hkl}^2\beta_{hkl}\cos\theta\right)$ on the X-axis is drawn as shown in Figure 3. Using the slope and intercept from the linearly fitted data, the mean crystallite size and the intrinsic strain of Fe_3O_4 nanoparticle is obtained. The estimated crystallite size and microstrain of the experimental as well as simulated data were found to be 23.28, 25.14 nm, and 2.79×10^{-8}, and 2.87×10^{-8}, respectively.

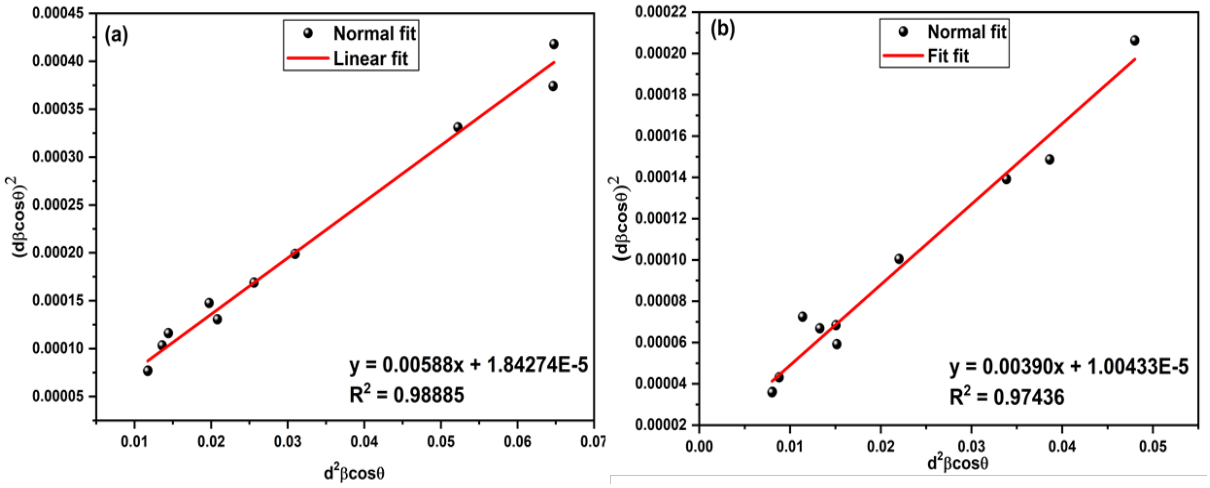

Figure 3: (a) Experimental Size-Strain Plot method estimated crystallite size of magnetite (Fe_3O_4) nanoparticle (b) Simulated Size-Strain Plot method estimated crystallite size of (Fe_3O_4) nanoparticles.

4.1.1.3 Halder-Wagner Method

The Halder-Wagner method is a widely used technique for estimating the crystallite size and microstrain of nanoparticles from X-ray diffraction (XRD) data. The method is based on the relationship between the crystallite size and the microstrain, which is given by the following equation (Khandan et al., 2014):

$$\beta_{hkl}^2 = \beta_L\beta_{hkl} + \beta_G^2 \quad (6)$$

where β is the FWHM of the diffraction peak, θ is the Bragg angle, λ is the wavelength of the X-ray radiation, D is the crystallite size, and ε is the microstrain. The Halder-Wagner method assumes that the spreading of the peak is a symmetric Voigt function, which means that the crystallite size and microstrain are estimated simultaneously

SLUJST
Sule Lamido University Journal of Science & Technology Vol. 9 No. 1&2 [May, 2024], pp. 184-196
https://doi.org/10.56471/
Online ISSN: 2736-0903
Print ISSN: 2736-089X
www.slujst.edu.ng

(Heryanto et al., 2019). In contrast, the Williamson-Hall method considers the effect of strain on the XRD peak broadening and can be used for the estimation of the intrinsic strain separated from the crystallite size. The Halder-Wagner method assumes that the crystallites are spherical and that the XRD peak profile is described by a linear combination of Lorentz and Gaussian functions. According to the Halder-Wagner method, the following formula describes the relationship between crystallite size and lattice strain (Patel et al., 2020):

$$\left(\frac{\beta^*_{hkl}}{d^*_{hkl}}\right)^2 = \frac{1}{D}.\frac{\beta^*_{hkl}}{d^{*\,2}_{hkl}} + \left(\frac{\varepsilon}{2}\right)^2 \quad (7)$$

where $d^*_{hkl} = 2d_{hkl}.\frac{\sin\theta}{\lambda}$. A linear plot will be obtained by plotting a graph of $\left(\frac{\beta^*_{hkl}}{d^*_{hkl}}\right)^2$ as the Y-axis and $\frac{\beta^*_{hkl}}{d^{*\,2}_{hkl}}$ as the x-axis for every XRD pattern. Figure 4 depicts the Halder-Wagner plots and linear least square equations derived from linear regression of plotted data. The average crystallite size is determined by the slope of the straight line, while the Fe_3O_4 nanoparticle's intrinsic strain is determined by the intercept value. From the graph, the estimated crystallite size and microstrain both the experimental as well as the simulated data were found to be 23.28, 25.14 nm, and 2.79×10^{-8}, 2.87×10^{-8} respectively. The average crystallite size and microstrain derived from the Halder-Wagner method are found to be consistent with models derived from the Scherer and Monshi-Scherer methods.

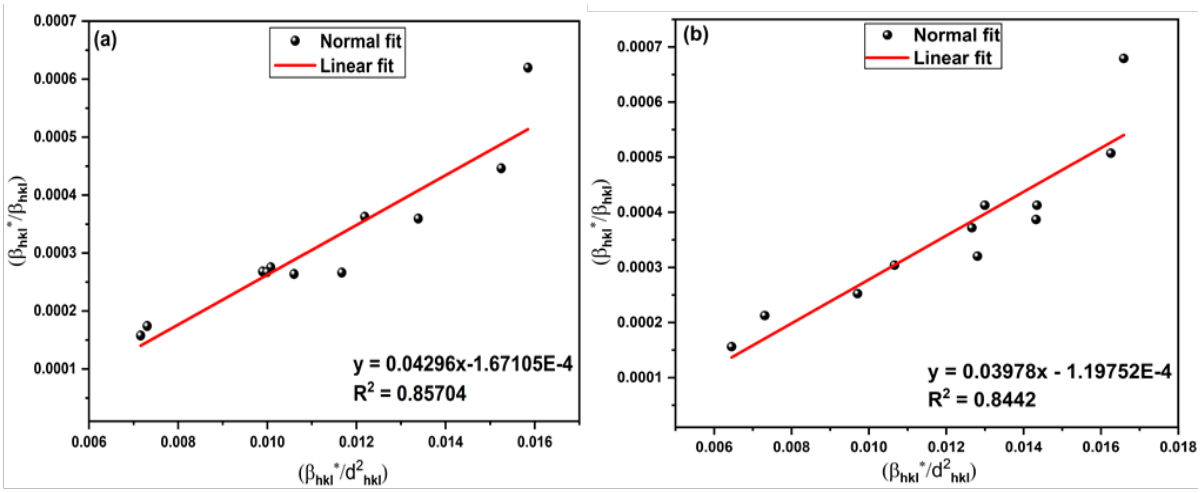

Figure 4: Halder Wagner method estimated crystallite size of magnetite (Fe_2O_3) nanoparticles.

4.1.2 X-ray Dispersive Spectroscopy (EDX)

Energy-Dispersive X-ray (EDX) analysis is a valuable technique employed to validate the composition of synthesized nanoparticles. In this research, EDX analysis was conducted to provide further confirmation regarding the composition of the obtained Fe_3O_4 nanoparticles. Notably, the focus of the analysis was on Fe_3O_4 nanoparticles. The results of the EDX spectra analysis, depicted in Figure 5, provide the chemical composition of the synthesized nanoparticles. The EDX spectra (Figure 4) clearly revealed the presence of oxygen (O) and iron (Fe) elements in the Fe_3O_4 nanoparticles (Kolluru et al., 2021). Importantly, no signals indicating the presence of other elements were detected, indicating the high purity of the synthesized Fe_3O_4 nanoparticles. The observed percentages of Fe and O in the EDX spectra closely matched the amounts of Fe and O utilized in the respective precursors (Mubarak et al., 2016). This correspondence provides strong evidence that no significant loss of elements occurred during the combustion process. It demonstrates the efficiency and effectiveness of the synthesis method employed in preserving the desired elemental composition during the production of Fe_3O_4 nanoparticles. Additionally, the presence of a minor peak for carbon (C) was observed in the EDX spectra. This peak can be attributed to the

Sule Lamido University Journal of Science & Technology Vol. 9 No. 1&2 [May, 2024], pp. 184-196
https://doi.org/10.56471/
Online ISSN: 2736-0903
Print ISSN: 2736-089X
www.slujst.edu.ng

presence of electric latex in the EDX sample holder (Chin et al., 2022b). These findings align with previous studies that have utilized EDX analysis to investigate the composition of Fe_3O_4 nanoparticles.

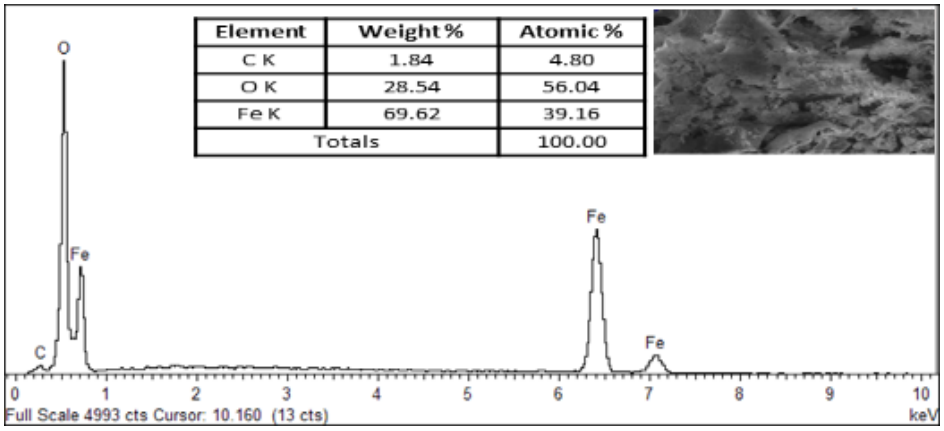

Figure 5: EDX spectra of magnetite (Fe_3O_4) nanoparticles.

4.1.3 Analysis of Magnetite (Fe_3O_4) Particle Size using Field Emission Scanning Electron Microscopy (FESEM)

Figure 6 depicts the FESEM images and size distribution histogram of Fe_3O_4 nanoparticles. The average particle size was estimated to be 39.52 nm. As evidently seen from Figure xx, the average particle size obtained using FESEM analysis exhibited a slight increase compared to the average crystallite size determined from experimental data, but it notably matched the average crystallite size derived from simulated data. The slightly larger average particle size estimated using FESEM analysis compared to the average crystallite size obtained from experimental data suggests potential factors such as particle aggregation or surface effects affecting FESEM measurements (Al-Tabbakh et al., 2019). However, its alignment with the average crystallite size derived from simulated data implies that the simulation captures the idealized crystalline structure more accurately, possibly overlooking such microstructural complexities evident in experimental measurements, thereby presenting a consistent estimate with FESEM analysis(Abd El-Sadek et al., 2019) .

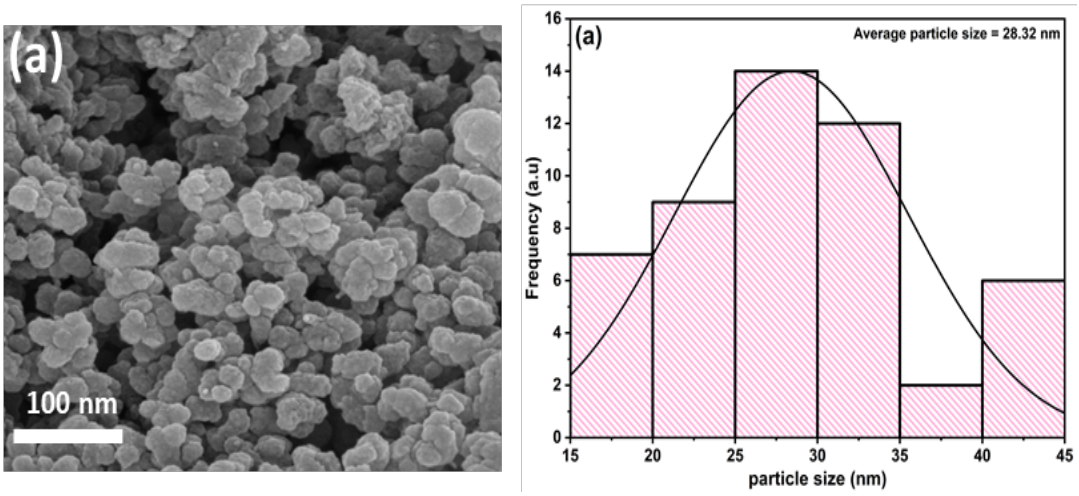

Figure 6: FESEM images and size distribution histogram of magnetite (Fe_3O_4) nanoparticles.

Sule Lamido University Journal of Science & Technology Vol. 9 No. 1&2 [May, 2024], pp. 184-196
https://doi.org/10.56471/
Online ISSN: 2736-0903
Print ISSN: 2736-089X
www.slujst.edu.ng

4.1.4 Analysis of Magnetite (Fe_3O_4) Particle Size using Transmission Electron Microscopy (TEM)

To further validate the estimated crystallite size using experimental as well as simulated data, transmission electron microscopy (TEM) was further used to determine the particle size. As depicted in Figure 7, the average particle size was found to be 40.23 nm. The estimated average particle size obtained is a bit greater than the average crystallite size estimated using the experimental data, but almost in agreement with the estimated average crystallite size of Fe_3O_4 nanoparticle estimated from the simulated data. The discrepancy between experimentally obtained average particle size and crystallite size, compared to simulated data, likely stems from differences in measurement techniques, sample preparation, and material properties [42]. Experimental methods may be influenced by sample homogeneity and instrument limitations, while simulations often assume ideal conditions. Variability in crystallinity and material properties further contribute to the observed differences (Augustin et al., 2016) .

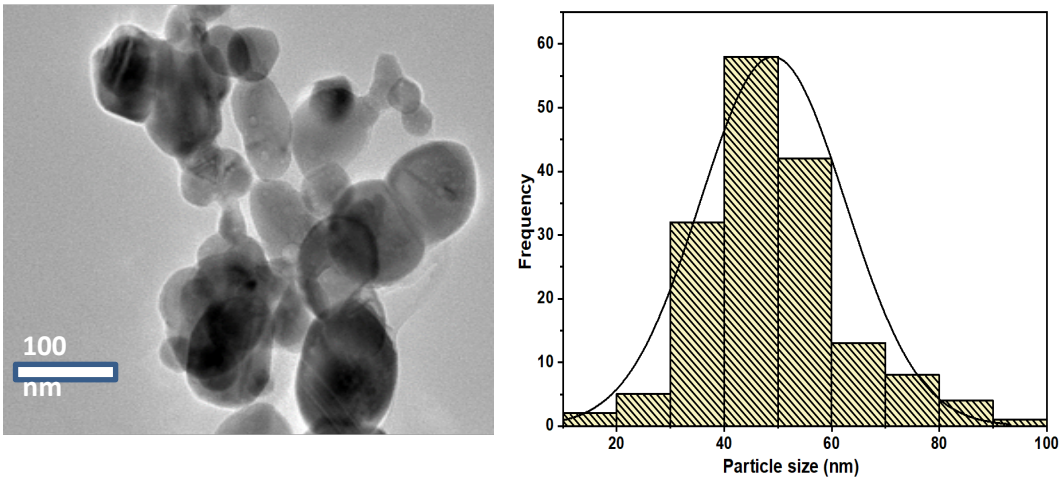

Figure 7: TEM images and size distribution histogram of magnetite (Fe_3O_4) nanoparticle

5. Conclusion

This research work explores the structural examination of synthesized magnetite (Fe_3O_4) nanoparticles by employing both experimental and simulated X-ray diffraction (XRD) methodologies. Through rigorous scrutiny, the investigation showcased the nanoparticles' high purity and crystallinity, which was supported by the close correspondence between experimental and simulated XRD patterns. Employing Scherer's method, Size Strain Plot method, and Halder-Wagner method, the study estimated the average crystallite size and microstrain of the nanoparticles. Discrepancies in the data between experimental and simulated approaches were identified, attributed to inherent variances in measurement techniques and material properties. Further validation of the nanoparticles' composition was provided by Energy-Dispersive X-ray (EDX) analysis, while particle size estimates were verified through transmission electron microscopy. This study offers comprehensive insights into the structural properties of Magnetite (FeO_4) nanoparticles. It underscores the importance of employing multiple analysis techniques and utilizing simulation methods to estimate the crystallite size of Fe_3O_4 nanoparticles. Through a combination of experimental approaches and simulations, the research provides a thorough understanding of the nanoparticles' composition and structural characteristics. By integrating findings from diverse methodologies, the study contributes to advancing knowledge in nanomaterials research and sets a groundwork for future investigations and applications in various fields.

Declaration of Competing Interest

Online ISSN: 2736-0903
Print ISSN: 2736-089X
www.slujst.edu.ng

The authors state that no conflicting financial interests or personal relationships may have influenced the results presented in this paper.

Acknowledgements

The authors extend their sincere gratitude to the Tertiary Education Trust Fund (TETFund) and the esteemed Bilyaminu Usman Polytechnic Hadejia, Jigawa State Nigeria, for their generous support and funding, which has been instrumental in facilitating the successful completion of this research work. Their unwavering commitment to advancing scientific exploration and innovation has played a pivotal role in enabling the exploration and discovery within this study. We truly appreciate their dedication to academic excellence and their invaluable contribution to the advancement of knowledge in our community and beyond.

References

Abd El-Sadek, M. S., Wasly, H. S., & Batoo, K. M. (2019). X-ray peak profile analysis and optical properties of CdS nanoparticles synthesized via the hydrothermal method. *Applied Physics A: Materials Science and Processing*, *125*(4). https://doi.org/10.1007/s00339-019-2576-y

Abed, A. H., Khodair, Z. T., Al-Saadi, T. M., & Al-Dhahir, T. A. (2019). Study the evaluation of Williamson-Hall (W-H) strain distribution in silver nanoparticles prepared by sol-gel method. *AIP Conference Proceedings*, *2123*. https://doi.org/10.1063/1.5116946

Adeniyi, A. G., Iwuozor, K. O., Emenike, E. C., Ajala, O. J., Ogunniyi, S., & Muritala, K. B. (2023). Thermochemical co-conversion of biomass-plastic waste to biochar: a review. In *Green Chemical Engineering*. KeAi Communications Co. https://doi.org/10.1016/j.gce.2023.03.002

Al-Tabbakh, A. A., Karatepe, N., Al-Zubaidi, A. B., Benchaabane, A., & Mahmood, N. B. (2019). Crystallite size and lattice strain of lithiated spinel material for rechargeable battery by X-ray diffraction peak-broadening analysis. *International Journal of Energy Research*, *43*(5), 1903–1911. https://doi.org/10.1002/er.4390

Aly, K. A., Khalil, N. M., Algamal, Y., & Saleem, Q. M. A. (2016). Lattice strain estimation for CoAl2O4 nano particles using Williamson-Hall analysis. *Journal of Alloys and Compounds*, *676*, 606–612. https://doi.org/10.1016/j.jallcom.2016.03.213

Aly, K. A., Khalil, N. M., Algamal, Y., & Saleem, Q. M. A. (2017). Estimation of lattice strain for zirconia nano-particles based on Williamson- Hall analysis. *Materials Chemistry and Physics*, *193*, 182–188. https://doi.org/10.1016/j.matchemphys.2017.01.059

Augustin, A., Rajendra Udupa, K., & Udaya Bhat, K. (2016). Crystallite size measurement and micro-strain analysis of electrodeposited copper thin film using Williamson-Hall method. *AIP Conference Proceedings*, *1728*. https://doi.org/10.1063/1.4946543

Basak, M., Rahman, M. L., Ahmed, M. F., Biswas, B., & Sharmin, N. (2022). The use of X-ray diffraction peak profile analysis to determine the structural parameters of cobalt ferrite nanoparticles using Debye-Scherrer, Williamson-Hall, Halder-Wagner and Size-strain plot: Different precipitating agent approach. *Journal of Alloys and Compounds*, *895*. https://doi.org/10.1016/j.jallcom.2021.162694

Bilal, M., Ihsanullah, I., Younas, M., & Ul Hassan Shah, M. (2022). Recent advances in applications of low-cost adsorbents for the removal of heavy metals from water: A critical review. In *Separation and Purification Technology* (Vol. 278). Elsevier B.V. https://doi.org/10.1016/j.seppur.2021.119510

Billah, A., Hossain, I., Nahar, A., Hasan, M., Roly, M. K., Anju, A. N., Saito, K., Hirose, F., Ahmmad, B., & Hoque, S. M. (2023). Enhanced magnetic and ferroelectric properties of La1−xMxFeO3 (M = Dy and Y) nanoparticles: A comparison of A-site doping. *Journal of Magnetism and Magnetic Materials*, *565*. https://doi.org/10.1016/j.jmmm.2022.170302

Chen, Y., Mao, W., Yang, W., Niazi, N. K., Wang, B., & Wu, P. (2023). A novel phosphate rock-magnetic biochar for Pb2+ and Cd2+ removal in wastewater: Characterization, performance and mechanisms. *Environmental Technology and Innovation*, *32*. https://doi.org/10.1016/j.eti.2023.103268

Chin, J. F., Heng, Z. W., Teoh, H. C., Chong, W. C., & Pang, Y. L. (2022a). Recent development of magnetic biochar crosslinked chitosan on heavy metal removal from wastewater – Modification, application and mechanism. In *Chemosphere* (Vol. 291). Elsevier Ltd. https://doi.org/10.1016/j.chemosphere.2021.133035

Online ISSN: 2736-0903
Print ISSN: 2736-089X
www.slujst.edu.ng

Chin, J. F., Heng, Z. W., Teoh, H. C., Chong, W. C., & Pang, Y. L. (2022b). Recent development of magnetic biochar crosslinked chitosan on heavy metal removal from wastewater – Modification, application and mechanism. In *Chemosphere* (Vol. 291). Elsevier Ltd. https://doi.org/10.1016/j.chemosphere.2021.133035

Desai, K. R., Alone, S. T., Wadgane, S. R., Shirsath, S. E., Batoo, K. M., Imran, A., Raslan, E. H., Hadi, M., Ijaz, M. F., & Kadam, R. H. (2021). X-ray diffraction based Williamson–Hall analysis and rietveld refinement for strain mechanism in Mg–Mn co-substituted CdFe2O4 nanoparticles. *Physica B: Condensed Matter*, *614*. https://doi.org/10.1016/j.physb.2021.413054

Dong, J., Shen, L., Shan, S., Liu, W., Qi, Z., Liu, C., & Gao, X. (2022). Optimizing magnetic functionalization conditions for efficient preparation of magnetic biochar and adsorption of Pb(II) from aqueous solution. *Science of the Total Environment*, *806*. https://doi.org/10.1016/j.scitotenv.2021.151442

Dongol, M., El-Denglawey, A., Abd El Sadek, M. S., & Yahia, I. S. (2015). Thermal annealing effect on the structural and the optical properties of Nano CdTe films. *Optik*, *126*(14), 1352–1357. https://doi.org/10.1016/j.ijleo.2015.04.048

Eltaweil, A. S., Ali Mohamed, H., Abd El-Monaem, E. M., & El-Subruiti, G. M. (2020). Mesoporous magnetic biochar composite for enhanced adsorption of malachite green dye: Characterization, adsorption kinetics, thermodynamics and isotherms. *Advanced Powder Technology*, *31*(3), 1253–1263. https://doi.org/10.1016/j.apt.2020.01.005

Gholizadeh, A. (2015). X-Ray Peak Broadening Analysis in LaMnO 3+δ Nano-Particles with RhombohedralCrystal Structure ARTICLE INFO ABSTRACT. In *Journal of Advanced Materials and Processing* (Vol. 3, Issue 3). www.SID.ir

Heryanto, Abdullah, B., Tahir, D., & Mahdalia. (2019). Quantitative analysis of X-Ray diffraction spectra for determine structural properties and deformation energy of Al, Cu and Si. *Journal of Physics: Conference Series*, *1317*(1). https://doi.org/10.1088/1742-6596/1317/1/012052

Jia, Y., Zhang, Y., Fu, J., Yuan, L., Li, Z., Liu, C., Zhao, D., & Wang, X. (2019). A novel magnetic biochar/MgFe-layered double hydroxides composite removing Pb 2+ from aqueous solution: Isotherms, kinetics and thermodynamics. *Colloids and Surfaces A: Physicochemical and Engineering Aspects*, *567*, 278–287. https://doi.org/10.1016/j.colsurfa.2019.01.064

Kandemir, T., Kasatkin, I., Girgsdies, F., Zander, S., Kühl, S., Tovar, M., Schlögl, R., & Behrens, M. (n.d.). *Microstructural and defect analysis of metal nanoparticles in functional catalysts by diffraction and electron microscopy: The Cu/ZnO catalyst for methanol synthesis*.

Khan, Z. H., Gao, M., Qiu, W., & Song, Z. (2020). Properties and adsorption mechanism of magnetic biochar modified with molybdenum disulfide for cadmium in aqueous solution. *Chemosphere*, *255*. https://doi.org/10.1016/j.chemosphere.2020.126995

Khandan, A., Karamian, E., & Bonakdarchian, M. (2014). Mechanochemical synthesis evaluation of nanocrystalline bone-derived bioceramic powder using for bone tissue engineering. *Dental Hypotheses*, *5*(4), 155–161. https://doi.org/10.4103/2155-8213.140606

Kolluru, S. S., Agarwal, S., Sireesha, S., Sreedhar, I., & Kale, S. R. (2021). Heavy metal removal from wastewater using nanomaterials-process and engineering aspects. In *Process Safety and Environmental Protection* (Vol. 150, pp. 323–355). Institution of Chemical Engineers. https://doi.org/10.1016/j.psep.2021.04.025

Kumar, S., Barman, P. B., & Raj Singh, R. (2021). Estimation and association of structural, elastic and magnetic properties of magnesium-nickel-ferrite nanoparticles annealed at different temperatures. *Materials Science and Engineering B: Solid-State Materials for Advanced Technology*, *272*. https://doi.org/10.1016/j.mseb.2021.115362

Kushwaha, P., & Chauhan, P. (2021). Microstructural evaluation of iron oxide nanoparticles at different calcination temperature by Scherrer, Williamson-Hall, Size-Strain Plot and Halder-Wagner methods. *Phase Transitions*, *94*(10), 731–753. https://doi.org/10.1080/01411594.2021.1969396

Liu, X., Zou, D., Liu, J., Zhou, C., & Zheng, B. (2020). Experimental study to evaluate the effect of particle size on the small strain shear modulus of coarse-grained soils. *Measurement: Journal of the International Measurement Confederation*, *163*. https://doi.org/10.1016/j.measurement.2020.107954

Online ISSN: 2736-0903
Print ISSN: 2736-089X
www.slujst.edu.ng

Monshi, A., Foroughi, M. R., & Monshi, M. R. (2012). Modified Scherrer Equation to Estimate More Accurately Nano-Crystallite Size Using XRD. *World Journal of Nano Science and Engineering*, *02*(03), 154–160. https://doi.org/10.4236/wjnse.2012.23020

Mubarak, N. M., Sahu, J. N., Abdullah, E. C., & Jayakumar, N. S. (2016). Plam oil empty fruit bunch based magnetic biochar composite comparison for synthesis by microwave-assisted and conventional heating. *Journal of Analytical and Applied Pyrolysis*, *120*, 521–528. https://doi.org/10.1016/j.jaap.2016.06.026

Mujtaba, M., Fernandes Fraceto, L., Fazeli, M., Mukherjee, S., Savassa, S. M., Araujo de Medeiros, G., do Espírito Santo Pereira, A., Mancini, S. D., Lipponen, J., & Vilaplana, F. (2023). Lignocellulosic biomass from agricultural waste to the circular economy: a review with focus on biofuels, biocomposites and bioplastics. In *Journal of Cleaner Production* (Vol. 402). Elsevier Ltd. https://doi.org/10.1016/j.jclepro.2023.136815

Patel, K., Chauhan, P., Patel, A. B., Solanki, G. K., Patel, K. D., & Pathak, V. M. (2020). Orthorhombic SnSe Nanocrystals for Visible-Light Photodetectors. *ACS Applied Nano Materials*, *3*(11), 11143–11151. https://doi.org/10.1021/acsanm.0c02301

Qu, J., Shi, J., Wang, Y., Tong, H., Zhu, Y., Xu, L., Wang, Y., Zhang, B., Tao, Y., Dai, X., Zhang, H., & Zhang, Y. (2022). Applications of functionalized magnetic biochar in environmental remediation: A review. In *Journal of Hazardous Materials* (Vol. 434). Elsevier B.V. https://doi.org/10.1016/j.jhazmat.2022.128841

Rani, N., Chahal, S., Chauhan, A. S., Kumar, P., Shukla, R., & Singh, S. K. (2019). X-ray Analysis of MgO Nanoparticles by Modified Scherer's Williamson-Hall and Size-Strain Method. In *Neha et al / Materials Today: Proceedings* (Vol. 12). www.sciencedirect.comwww.materialstoday.com/proceedings

Sapna, Budhiraja, N., Kumar, V., & Singh, S. K. (2018). X-ray Analysis of NiFe 2 O 4 Nanoparticles by Williamson-Hall and Size-Strain Plot Method . *Journal of Advanced Physics*, *6*(4), 492–495. https://doi.org/10.1166/jap.2017.1363

Shweta, G. M., Naik, L. R., Pujar, R. B., & Mathad, S. N. (2021). Influence of magnesium doping on structural and elastic parameters of Nickel Zinc nanoferrites. *Materials Chemistry and Physics*, *257*. https://doi.org/10.1016/j.matchemphys.2020.123825

Sonmez, M., Georgescu, M., Alexandrescu, L., Gurau, D., Ficai, A., Ficai, D., & Andronescu, E. (2015). SYNTHESIS AND APPLICATIONS OF Fe3O4/SiO2 CORE-SHELL MATERIALS. *Current Pharmaceutical Design*, *21*(37), 5324–5335. https://doi.org/10.2174/1381612821666150917094031

Vieira, L. H. S., Sganzerla Sabino, C. M., Soares Júnior, F. H., Rocha, J. S., Castro, M. O., Alencar, R. S., Souza da Costa, L., Viana, B. C., Jardim de Paula, A., Soares, J. M., Gomes Souza Filho, A., Otubo, L., Fechine, P. B. A., Ghosh, A., & Ferreira, O. P. (2020). Strategic design of magnetic carbonaceous nanocomposites and its application as multifunctional adsorbent. *Carbon*, *161*, 758–771. https://doi.org/10.1016/j.carbon.2020.01.089

Wang, L., Wang, J., Wang, Z., Feng, J., Li, S., & Yan, W. (2019). Synthesis of Ce-doped magnetic biochar for effective Sb(V) removal: Performance and mechanism. *Powder Technology*, *345*, 501–508. https://doi.org/10.1016/j.powtec.2019.01.022

Yang, F., Du, Q., Sui, L., & Cheng, K. (2021). One-step fabrication of artificial humic acid-functionalized colloid-like magnetic biochar for rapid heavy metal removal. *Bioresource Technology*, *328*. https://doi.org/10.1016/j.biortech.2021.124825

Yi, Y., Huang, Z., Lu, B., Xian, J., Tsang, E. P., Cheng, W., Fang, J., & Fang, Z. (2020). Magnetic biochar for environmental remediation: A review. In *Bioresource Technology* (Vol. 298). Elsevier Ltd. https://doi.org/10.1016/j.biortech.2019.122468

Yi, Y., Tu, G., Zhao, D., Tsang, P. E., & Fang, Z. (2019). Biomass waste components significantly influence the removal of Cr(VI) using magnetic biochar derived from four types of feedstocks and steel pickling waste liquor. *Chemical Engineering Journal*, *360*, 212–220. https://doi.org/10.1016/j.cej.2018.11.205

Yousefi, S., Ghasemi, B., & Nikolova, M. P. (2022). Morpho/Opto-structural Characterizations and XRD-Assisted Estimation of Crystallite Size and Strain in MgO Nanoparticles by Applying Williamson–Hall and Size–Strain Techniques. *Journal of Cluster Science*, *33*(5), 2197–2207. https://doi.org/10.1007/s10876-021-02144-y

Online ISSN: 2736-0903
Print ISSN: 2736-089X
www.slujst.edu.ng

Zahedifar, M., Seyedi, N., Shafiei, S., & Basij, M. (2021). Surface-modified magnetic biochar: Highly efficient adsorbents for removal of Pb(II) and Cd(II). *Materials Chemistry and Physics*, *271*, 124860. https://doi.org/10.1016/j.matchemphys.2021.124860

Zhou, R., Huang, Y., Zhou, J., Niu, H., Wan, L., Li, Y., Xu, J., & Xu, J. (2018). Copper selenide (Cu3Se2 and Cu2−xSe) thin films: electrochemical deposition and electrocatalytic application in quantum dot-sensitized solar cells. *Dalton Transactions*, *47*(46), 16587–16595. https://doi.org/10.1039/c8dt03791d